ACS central science

http://pubs.acs.org/journal/acscii

Research Article

Periodic Arrays of Chiral Domains Generated from the Self-Assembly of Micropatterned Achiral Lyotropic Chromonic Liquid Crystal

Geonhyeong Park,[¶] Simon Čopar,[¶] Ahram Suh, Minyong Yang, Uroš Tkalec,[*] and Dong Ki Yoon[*]

Cite This: https://dx.doi.org/10.1021/acscentsci.0c00995

Read Online

ACCESS | Metrics & More | Article Recommendations | Supporting Information

ABSTRACT: Achiral building blocks forming achiral structures is a common occurrence in nature, while chirality emerging spontaneously from an achiral system is usually associated with important scientific phenomena. We report on the spontaneous chiral symmetry-breaking phenomena upon the topographic confinement of achiral lyotropic chromonic liquid crystals in periodically arranged micrometer scale air pillars. The anisotropic fluid arranges into chiral domains that depend on the arrangement and spacing of the pillars. We characterize the resulting domains by polarized optical microscopy, support their reconstruction by numerical calculations, and extend the findings with experiments, which include chiral dopants. Well-controlled and addressed chiral structures will be useful in potential applications like programmable scaffolds for living liquid crystals and as sensors for detecting chirality at the molecular level.

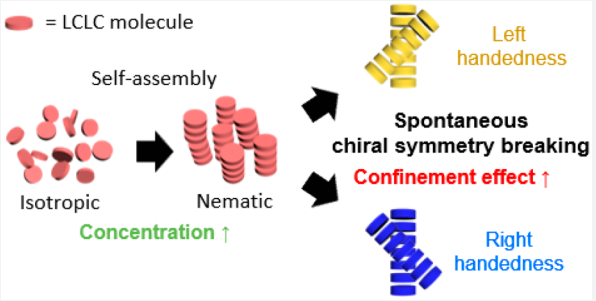

INTRODUCTION

Since Pasteur studied the optical activity of tartaric acid,[1] chiral objects in chemistry and material sciences have been of keen interest in supramolecular assembly,[2] catalysis,[3] and optics.[4] Chiral characteristics result from chiral moieties in molecules[2−4] or axial chirality of different molecular planes,[5] which have been massively studied. However, the chiral symmetry breaking of supramolecular assemblies is not clearly understood; however, it is important for the purposes of practicality and as a clue to solve the evolution of life.[6]

In terms of this viewpoint, liquid crystals (LCs) that are sensitive to external fields such as geometrical confinement and electrical, mechanical, and chemical perturbations are fascinating materials, which have been extensively studied in the past decades.[7−10] For instance, chiral symmetry breaking happens when LC molecules have bent shapes[11−13] or are placed in confined geometries.[14−17] Among the various kinds of LC types, lyotropic chromonic LCs (LCLCs), dissolved in water, are frequently used to explore spontaneous chiral symmetry breaking.[18−23] LCLC molecules have rigid planar shapes due to polyaromatic cores, which spontaneously aggregate "face-to-face" through $\pi-\pi$ stacking interaction to form columns when they are dissolved in an aqueous medium. At a low concentration, the LCLC aggregates are short and oriented randomly, which is the isotropic (Iso) state. As the concentration increases, the length of the columns increases, and the nematic (N) phase with long-range orientational order appears.[24] Due to the semiflexible polymer-like behaviors, this type of nematic LC (NLC) has an order of magnitude lower twist elastic constant (K_2) when compared to splay (K_1) and bend (K_3) elastic constants.[25,26] Precise control of the elastic deformation of NLCs and the surface anchoring of confined geometries are essential to induce chiral symmetry breaking and to command the orientational patterns on templated surface topographies.[27−30] However, in previous studies,[18−23] the handedness of twisted domains and specific locations, in which chiral domains were formed, has not been well-controlled and scaled to large areas, and only the spontaneous emergence of domains was observed. In order to use the chiral structures of LCLC materials for sensor[31,32] or optical[33−35] applications fabricated by conventional chiral LC materials or solitonic structures in chiral nematic phases,[33−35] precise control of the handedness and microscopic placement of chiral domains is essential. In this study, we adopt micropatterned silicon wafers to induce periodically well-addressed air pillars,[36] which can induce a complete degenerate anchoring condition and periodic confinement effects on a millimeter scale. In addition, a diamond lapping scratch method was introduced to fabricate nanogrooves[37] on the wafers, which can control the orientation of conventional LCLC materials, disodium cromoglycate (DSCG) in this case. Spontaneously generated

Received: July 28, 2020

chiral domains from achiral DSCG molecules are well-controlled by a competitive interaction between the surface anchoring condition of confined geometries and the elasticity of LCLC. These periodically generated domains are directly investigated by polarized optical microscopy (POM) and analyzed using theoretical interpretation and numerical calculations. The behavior is verified by experimentally comparing the homochiral structures generated with specific chiral additives, which suggests a way to control the handedness of chiral domains both in our system and similar systems in biophysics.

RESULTS AND DISCUSSION

Generation of Periodic Chiral Domains Using Surface Anchoring Anisotropy. To generate periodic chiral domains, first, the cylindrical holes with a 20 μm diameter, a 5 μm depth, and a 20 μm spacing arranged in a square lattice (Figure 1a and b) were fabricated on a silicon wafer using conventional lithographic techniques. The micropatterned wafer was sandwiched with a pristine glass substrate, and the assembled LC cell gap was fixed with 2 μm diameter silica microspheres. Then, DSCG, dissolved in deionized water at 15 wt %, was injected slowly at room temperature. Capillary action took place inside the LC cell, but the DSCG solution did not fill the patterned area where pillar-like air cavities were spontaneously generated above the intaglio holes (Figure 1c and d). After injecting the DSCG solution, the LC cell was heated to the Iso state at 45 °C and slowly cooled down to 25 °C, which is the N phase temperature, to erase the shear-aligning effect of the injection process. The colorful texture of the thin DSCG layer was observed by POM with a 530 nm (λ) wave plate, inserted at 45° with respect to the polarizers (red line in Figure 1d). When the long axis of DSCG columns, the director $\boldsymbol{n}$, is parallel or perpendicular to either of the crossed polarizers or when the sample is in the Iso state, a magenta color is observed. When $\boldsymbol{n}$ is parallel or perpendicular to the slow axis of the λ wave plate, the sample shows a yellow or blue interference color, respectively.[38] In Figure 1d, the DSCG texture shows randomly oriented $\boldsymbol{n}$ because neither the glass nor silicon substrate could induce the preferred orientation. The unidirectional orientation of $\boldsymbol{n}$ can be achieved with nanogrooves formed by the diamond scratching method[37] on a micropatterned wafer (green arrow in Figure 1e–g), in which the top glass substrate retains degenerate planar anchoring. The conventional rubbed polymer alignment layer does not work well in our system due to the wetting problem and the low surface anchoring energy of DSCG.[39] Following the procedure above, a new cell was filled with the DSCG solution and thermally treated. Now, a dramatic change of the textures in the POM images (Figure 1g and h, Video 1) was observed. Most of the sample aligned unidirectionally along the nanogrooves, only the director field near the air pillars showed distortions. According to the POM image analysis in Figure 1h, the LCLC oriented tangentially around the surface of the air, showing that the air imposes a planar anchoring condition on the DSCG columns; however, air gives conventional thermotropic LCs a homeotropic alignment.[36] The resultant textures are similar to distortions around spherical colloids in previous research,[19,40] but here, chiral tails are not present in the N state (Figure 1g and h).

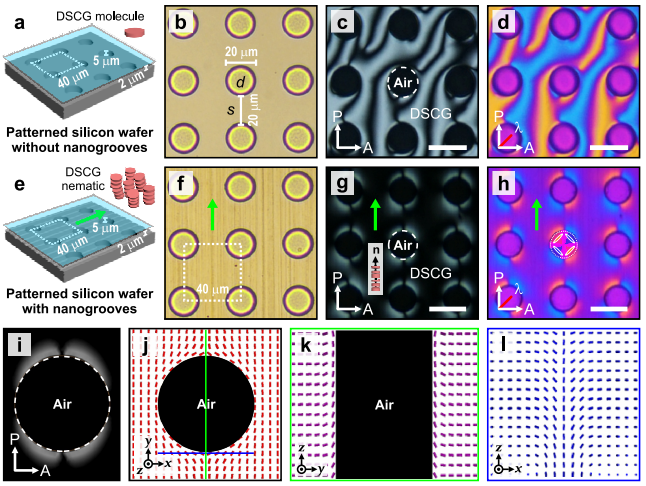

Figure 1. Substrate patterns and the resulting nematic textures. (a) Schematic illustration of a patterned silicon wafer, LC cell design with dimensions, and DSCG molecule. (b) Optical microscope image of the patterned silicon wafer with cylindrical hole pattern, which has a 20 μm diameter, a 5 μm height, and a 20 μm spacing. (c and d) POM images (without and with the λ wave plate) of a 15 wt % DSCG water solution in the cell with a patterned silicon wafer. (e) Schematic illustration of a patterned silicon wafer with nanogrooves, cell design, and columns of the DSCG molecules. (f) Optical microscope image of the patterned silicon wafer with nanogrooves and with the same pattern as in panel b. (g and h) POM images (without and with the λ wave plate) of a 15 wt % DSCG water solution in the cell with a patterned silicon wafer with nanogrooves. (i) Corresponding POM texture, simulated by the Jones matrix formalism. (j–l) Average in-plane director configuration in the (j) xy plane, followed by cross-section director configurations in the (k) yz and (l) xz planes. White crossed arrows indicate the polarizer and analyzer direction, the red arrow indicates the slow axis of the λ wave plate, and the green arrow indicates the direction of nanogrooves throughout the paper. Scale bars = 30 μm.

Numerical simulation, based on the Frank–Oseen free energy,[41] was conducted to investigate the spontaneous chiral symmetry breaking and the energetically favorable director configuration near the air surface (see Experimental Section):

$$F_{\text{total}} = \int \frac{1}{2}K_1(\nabla\cdot n)^2 + \frac{1}{2}K_2(n\cdot\nabla\times n)^2 + \frac{1}{2}K_3(n\times\nabla\times n)^2 dV = F_{\text{splay}} + F_{\text{twist}} + F_{\text{bend}} \quad (1)$$

The simulated image (Figure 1i) is in good agreement with the experimental result (Figure 1g). The average in-plane director configuration of the simulated data (Figure 1j) is also in agreement with the observation in Figure 1h. As shown in the yz cross-section profile (Figure 1k), $\boldsymbol{n}$ is aligned vertically in contact with the air surface. The vertical escape points at the air surface (see the crossing of the green and blue line in Figure 1j) resulted from an interplay of degenerate planar anchoring at the LC–air interface, cylindrical curvature of the air, and uniform planar anchoring at the bottom substrate. To the left and the right of the vertical escape, oppositely handed twisted domains are observed, as shown in the yz profile of Figure 1l. The blue-colored region in Figure 1h and l was twisted with right-handedness, and the yellow region was twisted with left-handedness along the $+z$ direction. According to previous research,[28] the surface anchoring energy (W) of the bottom silicon wafer with nanogrooves, which can align LCLC materials perfectly, is 10^{-5} J/m^2 < W_{bottom} < 10^{-4} J/m^2. The extrapolation length (L) of the bottom substrate for DSCG is $L_{\text{bottom}} \approx K_2/W_{\text{bottom}} < 10^{-6}$ μm, which is smaller than the LC

https://dx.doi.org/10.1021/acscentsci.0c00995
ACS Cent. Sci. XXXX, XXX, XXX–XXX

cell gap of 2 μm; K_2 is less than $K' \approx 10$ pN, which is an estimated elastic constant for DSCG in the N phase.[42] Therefore, $\boldsymbol{n}$ in the lower part of the cell was aligned uniaxially, following the direction of the nanogrooves. In contrast, $\boldsymbol{n}$ in the upper part of the cell obeyed the degenerate planar anchoring of the air and top glass, which is less restrictive and allows deviations from the bottom director governed by the nanogroove direction.

Interaction between Chiral Domains. For microspheres dispersed in chromonic LC, it was experimentally demonstrated that colloidal particles induce bipolar director configurations, attract, and arrange at 30° with respect to the LC alignment direction.[19,43] To investigate the attractive interaction between locally formed chiral domains, the square lattice was changed to the hexagonal lattice with the same hole size and separation as in Figure 1 (see Figure 2a). Similar to the elastic colloidal assembly, the interaction between domains was observed in the space between adjacent air pillars (white dashed area in Figure 2b). A notable difference from the previous study[19,43] is that instead of movable spheres, fixed cylindrical air pillars provide a regular lattice to support the director pattern. We see that the chiral domains, induced by the anchoring at the surface of the air pillars (Figure 1l), extend from the air interface toward like-handed domains on the neighboring pillars and interact with them. The characteristic length (ξ) of the domain, and thus the reach of the interdomain interaction, is set by

$$\xi_{\text{domain}} = \frac{h}{\sqrt{3}}\sqrt{K/K_2} \tag{2}$$

where h is the cell thickness and $K = \frac{1}{2}(K_1 + K_3)$. It shows that a low twist elastic constant is essential for allowing long-range interactions between domains.

To further explore the creation of connected chiral domains between adjacent pillars, a square lattice with a narrower pillar-to-pillar spacing was prepared (Figure 2c and d). The sequential changes in cooling from the Iso state provided an additional insight into the nucleation of the domains (Figure 2e, Video 2). During the Iso−N phase transition, the N regions nucleate and grow from the air surface, revealing oval shapes with a tangentially aligned director configuration (Figure 2e). When the neighboring domains meet, the elliptical shapes are merged in a particular direction, along the nanogrooves (green arrow in Figure 2e). A numerical analysis was conducted to analyze the director field in the same way as before.[41] The simulated POM image in Figure 2g is in good agreement with the experimental POM image in Figure 2f. The chiral domains consist of a twisting director (see the cross-section in Figure 1l) from the nanogroove-aligned director at the bottom to an angled director at the top, which is enforced by the planar anchoring at the nearby air interface. Larger domains are formed when domains of the same chirality merge between neighboring air pillars. In this case, as there was no preferential direction, the handedness of connected domains was determined by an uneven cooling at the nucleation and growth process. Therefore, blue (right-handed) and yellow (left-handed) domains were connected randomly (colors are seen in the experimental POM images, e.g., Figure 2d). The proposed structure is confirmed by simulations in Figure 2g.

The free energy of the region of interest between the pillars (dashed box in Figure 2g) is visualized in Figure 2h, split into elastic contributions according to Equation 1. We see that twist deformation dominates in the middle of the connected domain, suppressing the more expensive bend and splay deformation. Regions of high deformation are offset from the center in opposite directions at both pillars (see positions *i* and *ii* in Figure 2g), indicating repositioning of the vertical escape points. In a simplified sense, the director angle can be thought to be parallel to the substrate and changes from 0° with respect to the nanogrooves at the bottom to the maximum angle $\varphi(x, y)$ at the top plate. Neglecting the twist deformation, which has a much lower elastic constant, we obtain a Laplace equation $\nabla^2\varphi = 0$ for the angle at the top plate, which is trivially solved if the boundary conditions are known. Figure 2i shows solutions for the top angle at different positions where the director at the surface is not tangential to the substrate. This simulation shows that symmetry breaking is catalyzed by the mobility of these vertical escape points, points of nonplanarity. The defects deflect away from each other on neighboring air pillars, making room for two like-handed domains to connect.

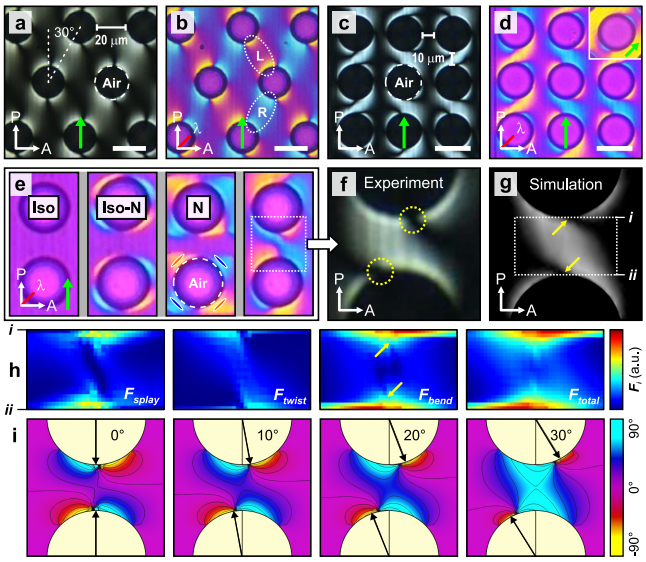

Figure 2. Chiral domain formation between the air pillars. (a and b) POM images (without and with the λ wave plate) of the DSCG in a cell with a hexagonal hole pattern on the silicon substrate. In the domains, the nematic LCLC forms a left- (L) and a right- (R) handed twist perpendicular to the substrate. (c and d) POM images (without and with the λ wave plate) of the nematic texture, formed on a denser square hole pattern. Note that the domains between the neighboring air pillars are different, i.e., left- (yellow) or right- (blue) handed, chosen randomly through spontaneous symmetry breaking. The inset in panel d shows an image that the sample is reoriented by 45° with respect to the polarizers. (e) The growth of the domains during the Iso−N transition. The domains nucleate at the air pillars, and the symmetry breaking happens when the nematic islands coalesce. (f and g) Comparison between experimental and simulation images of a single chiral domain. Observe the black brushes connecting to the surface where the director does not lie in the plane of the substrate, which we call vertical escape points (dashed yellow circles). They deflect from the symmetric central position, breaking the symmetry. (h) Localization of high deformation energy, splay, twist, bend, and total, within the outlined region in panel g. (i) A set of analytical schematics of the deflection angle between the director and the nanogrooves at the top glass surface, showing that the symmetry breaking occurs through shifting of the vertical escape point position. Scale bars = 30 μm.

https://dx.doi.org/10.1021/acscentsci.0c00995
ACS Cent. Sci. XXXX, XXX, XXX−XXX

Measurements of these angles of deflection are presented in Figure 3f.

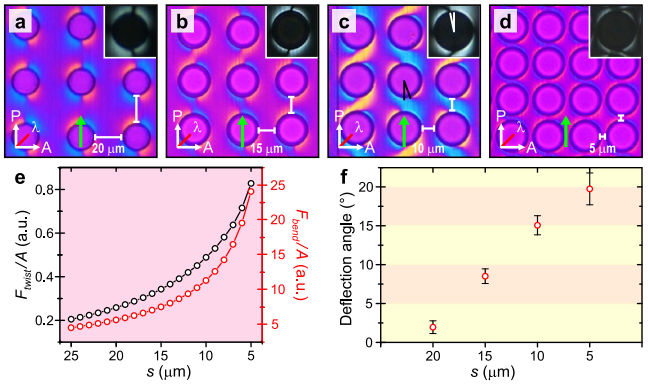

Figure 3. symmetry-breaking variation with interpillar spacing. (a–d) The deflection angles of the vertical escape points (black positions at the surface of the pillar, additionally marked in (c)) increase when the distance between the pillars is decreased from 20 μm (a) to 15 μm (b), 10 μm (c), and 5 μm (d). (e) Normalized elastic free-energy contribution of the bend deformation (red) and the twist deformation (black). As the distance decreases, the free energy of each deformation increases. (f) The dependence of the deflection angles with respect to the interpillar spacing. The distribution of the angles is broader due to the increase of the elastic free energy when the spacing is smaller.

Control of Chiral Domains with Confinement Variation. The bend deformation in the connected domains is related to the distance between neighboring air pillars. At s = 20 μm (Figure 3a), little interaction between the chiral domains was observed. As s decreased to 15 μm (Figure 3b, Video 3) and 10 μm (Figure 3c, Video 2), the interaction between domains became stronger. At s = 5 μm (Figure 3d, Video 4), the domain spacing became too short, so merged domains were observed not only parallel to the nanogroove direction but also perpendicular to it. To quantitatively compare this scaling with s, F_{Bend} and F_{Twist} were calculated and normalized with a unit area A at the same position as the white box in Figure 2g (see Figure 3e). F_{splay} was almost constant in the range of 5 to 25 μm, meaning that splay deformation only occurs around the air surface with relatively little involvement in the formation of twist domains. In Figure 3e, it could be observed that as s decreased from 25 to 5 μm, both F_{Twist}/A (black) and F_{Bend}/A (red) increased with the characteristic length (ξ), consistent with the analytical estimate $\xi_{domain} \approx 5.7$ μm (detailed in Experimental Section).

The increase of F_{Twist}/A resulted from some of the bend deformation relaxing into twist deformation due to the lower elastic cost of twist compared to bend deformation. This is achieved through an increase of the deflection angle of vertical escape point positions. The deflection angles between the nanogrooves direction and the pillar center, vertically escaped point lines, were measured for each spacing (5 to 20 μm) to quantify this effect (Figure 3f). The trend of an increasing deflection angle with a narrowing of the interpillar gap is consistent with the growth of twist and bend energy (Figure 3e).

Control of Chiral Domains with Chemical Additives. To confirm whether the resultant structures are chiral or not, control experiments were carried out, in which chiral dopants were added to the DSCG solution to make either left- or right-handed domains. We applied L-alanine and D-alanine, which are commonly used to make LCLCs homochiral.[44] As shown in the results above, domain handedness is reflected in yellow- and blue-colored regions (Figure 4b, Video 2). In racemic

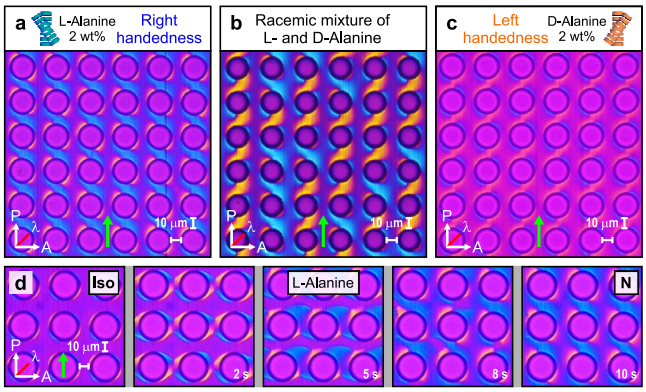

Figure 4. Control of the racemic domain handedness with the addition of chiral dopants. (a–c) POM images with an inserted λ wave plate of a LCLC solution with the addition of (a) 2 wt % L-alanine, (b) a racemic mixture of L-alanine and D-alanine, and (c) 2 wt % D-alanine in nanogrooved square lattice patterns. An enantiomeric excess induced by alanine amplifies a specific handedness of chiral domains such that only one type of domain is revealed. (d) A sequence of right-handed domain formation during the Iso–N transition of a 2 wt % L-alanine-doped DSCG solution. The amplification of a right-handed domain by an enantiomeric excess can be observed during the Iso–N transition.

mixtures, the domains are randomly determined during cooling, as there is no preference for a specific handedness. However, the optical textures become completely ordered when homochiral molecules were added to the DSCG solution. In the LC cell of L-alanine-added DSCG, only blue-connected domains appeared (Figure 4a, Video 5), while only yellow ones were revealed with D-alanine-doped DSCG (Figure 4c, Video 6). This outcome experimentally demonstrated our argument that the surface chirality generated from surface anisotropy was expanded to the broader area described above. In contrast to the cooling from the Iso to the N phase of the achiral mixture (Figure 2e), Figure 4d shows that, for L-alanine-doped DSCG, germs of right-handed domains grow larger even before merging, leading to uniformly right-handed domains.

Safety Statement. No unexpected or unusually high safety hazards were encountered throughout experimentation.

CONCLUSION

We successfully fabricated a periodic array of chiral domains based on anisotropic surface anchoring conditions and the elasticity of the LCLC. The resultant chiral symmetry-breaking platform suggests a new route to build a well-controlled three-dimensional director configuration of supramolecular LCLCs, which is comparable with the conventional two-dimensional system.[27−30] Indeed, this uses topographical patterns fabricated by well-known lithographic techniques, enabling the employment of parallel processes to generate the chiral domains on demand. These findings are closely related to potential programmable scaffolds, e.g., for controlling living active materials[45] and chiral assemblies of plasmonic particles[46] and investigating chiral fluid behaviors.[40,47]

https://dx.doi.org/10.1021/acscentsci.0c00995
ACS Cent. Sci. XXXX, XXX, XXX−XXX

EXPERIMENTAL SECTION

Sample Preparation and Characterization. Disodium cromoglycate (DSCG, > 95%), purchased from Sigma-Aldrich, was dissolved in deionized water at a 15 wt % concentration without any further purification. Chiral dopants, D-alanine and L-alanine, purchased from Alfa Aesar, were added to a 15 wt % DSCG solution at a 2 wt % concentration without any further purification.

Various micropatterned silicon wafers were fabricated on (100) wafers with conventional photolithography and reactive ion etching techniques. Nanogrooves were fabricated on the micropatterned wafer by nanoscratching techniques.[37] The surface of the patterned wafers was scratched with 500 nm diamond lapping films, purchased from Allied High Tech Products. The applied pressure on the silicon substrate during scratching was ∼1.18 N/cm^2, and the scratching velocity was ∼1.9 cm/s. These wafers and pristine glass were cleaned using acetone, ethanol, and deionized water, and were finally treated with O_2 plasma for 5 min to eliminate organic impurities. The substrates were sandwiched with 2 μm silica microspheres as spacers and UV curable adhesives. The 15 wt % DSCG solution was injected slowly into the sandwich cell by capillary action. To erase flow-induced alignment, cells were heated to 45 °C with a heating stage (Linkam LTS420) and cooled to 25 °C. Optical textures of the nematic DSCG solution were measured using POM (Nikon Eclipse LV100POL) with a 530 nm (λ) wave plate and imaged with a charge-coupled device camera (Nikon DS-Ri1). Deflection angles in Figure 3f were measured based on POM images by using the image process program ImageJ (LOCI, University of Wisconsin).

Numerical Simulation. The dimensionless free energy to be minimized consists of the bulk elastic energy F_{total} (see Equation 1) and surface anchoring contributions $F_{surface} = \frac{1}{2}(W(1 - \mathbf{n}\cdot\mathbf{n_r}))$ where $\mathbf{n}$ is the Cartesian director $\mathbf{n} = (n_x, n_y, n_z)$, $\boldsymbol{n}^2 = n_x^2 + n_y^2 + n_z^2 = 1$, and $\mathbf{n_r}$ is the prealigned direction. K_1, K_2, and K_3 correspond to splay, twist, and bend deformations, respectively, which is a method used in previous research.[41] Elastic constants for the nematic DSCG are K_1 = 10 pN, K_2 = 0.7 pN, and K_3 = 24 pN, respectively.[23,24] Surface anchoring energies were used for pristine glass, $W_{top} = 10^{-7}$ J/m^2, with degenerate planar anchoring conditions and for a silicon wafer with nanogrooves, $W_{bottom} = 10^{-5}$–10^{-4} J/m^2.[28,39] Saddle-splay elasticity was ignored because the LC cell had too short of a gap, and any textures that have to be shown in a positive curvature were not observed in experimental data (Figure 2e). On the basis of this method and constants, the calculation was conducted on a square lattice with commercially available software (Techwiz, LCD 3D, Sanayi System Company). In Figure 1j and k, a three-dimensional director configuration was extracted from the calculated results. Simulated POM images in Figure 1i and Figure 2g were obtained by 2 × 2 Jones matrices.

The free energy in eq 1 can be simplified with an ansatz of a planar director $\mathbf{n} = (\cos(\varphi z/h), \sin(\varphi z/h), 0)$, only depending on x and y, where h is the cell thickness. Assuming $K_1 = K_3$ and neglecting K_2 allows us to derive a Euler–Lagrange equation in the form of a Laplace equation, $\nabla^2\varphi(x, y) = 0$. The Laplace equation was solved numerically with Mathematica 11 (Wolfram Research), with boundary conditions at the surface of pillars matching the tangent to the pillar cross-section. The boundary condition has a π jump at the position of the vertical escape point, which we varied by adjusting the boundary condition.

If K_2 is not ignored, we obtain a better approximation of the free energy per unit of area:

$$F_{total}/A \approx \frac{1}{2}K\left(\frac{h}{3}\right)(\nabla\varphi)^2 + \frac{1}{2}K_2\left(\frac{1}{h}\right)\varphi^2 \quad (3)$$

with $K = \frac{1}{2}(K_1 + K_3)$, which leads to the characteristic length of the chiral domain, $\xi_{domain} = \frac{h}{\sqrt{3}}\sqrt{K/K_2} \approx 5.7$ μm.

ASSOCIATED CONTENT

Supporting Information

The Supporting Information is available free of charge at https://pubs.acs.org/doi/10.1021/acscentsci.0c00995.

Descriptions of the videos with experimental details, as noted in the text (PDF)

Video S1: 20 μm (AVI)

Video S2: 10 μm (AVI)

Video S3: 15 μm (AVI)

Video S4: 5 μm (AVI)

Video S5: L-alanine, 10 μm (AVI)

Video S6: D-Alanine, 10 μm (AVI)

AUTHOR INFORMATION

Corresponding Authors

Uroš Tkalec − *Institute of Biophysics, Faculty of Medicine, University of Ljubljana, 1000 Ljubljana, Slovenia; Faculty of Natural Sciences and Mathematics, University of Maribor, 2000 Maribor, Slovenia; Department of Condensed Matter Physics, Jožef Stefan Institute, 1000 Ljubljana, Slovenia*; Email: uros.tkalec@mf.uni-lj.si

Dong Ki Yoon − *Graduate School of Nanoscience and Technology and Department of Chemistry and KINC, Korea Advanced Institute of Science and Technology, Daejeon 34141, Republic of Korea*; orcid.org/0000-0002-9383-8958; Email: nandk@kaist.ac.kr

Authors

Geonhyeong Park − *Graduate School of Nanoscience and Technology, Korea Advanced Institute of Science and Technology, Daejeon 34141, Republic of Korea*

Simon Copar − *Faculty of Mathematics and Physics, University of Ljubljana, 1000 Ljubljana, Slovenia*

Ahram Suh − *Graduate School of Nanoscience and Technology, Korea Advanced Institute of Science and Technology, Daejeon 34141, Republic of Korea*

Minyong Yang − *Graduate School of Nanoscience and Technology, Korea Advanced Institute of Science and Technology, Daejeon 34141, Republic of Korea*

Complete contact information is available at: https://pubs.acs.org/10.1021/acscentsci.0c00995

Author Contributions

¶G.P. and S.Č. contributed equally to this work. G.P. and D.K.Y. designed the research. G.P. performed the experiments and analysis. S.Č. and U.T. performed the theoretical analysis of the system. A.S. and M.Y. helped with experiments. U.T. and D.K.Y. supervised the research. All authors analyzed the experimental data and wrote the manuscript.

https://dx.doi.org/10.1021/acscentsci.0c00995
ACS Cent. Sci. XXXX, XXX, XXX−XXX

Notes

The authors declare no competing financial interest.

■ ACKNOWLEDGMENTS

This work was supported by the National Research Foundation of Korea (NRF), grant-funded by the Korean Government (MSIT) under Grant Nos. 2017R1E1A1A01072798, 2019K1A3A1A14065772, and 2018R1A5A1025208. This research was additionally supported by the Slovenian Research Agency (ARRS) through research core funding No. P1-0099 to S.Č. and No. P1-0055 to U.T., and S.Č. and U.T. would like to acknowledge the contribution of the COST Action CA17139.

■ REFERENCES

(1) Pasteur, L. Recherches sur les relations qui peuvent exister entre la forme crystalline, la composition chimique et le sens de la polarisation rotatoire. *Ann. Chim. Phys.* **1848**, *24*, 442−459.
(2) Cornelissen, J. J. L. M.; Rowan, A. E.; Nolte, R. J. M.; Sommerdijk, N. A. J. M. Chiral Architectures from Macromolecular Building Blocks. *Chem. Rev.* **2001**, *101* (12), 4039−4070.
(3) Noyori, R. Asymmetric Catalysis: Science and Opportunities (Nobel Lecture). *Angew. Chem., Int. Ed.* **2002**, *41* (12), 2008−2022.
(4) Brandt, J. R.; Salerno, F.; Fuchter, M. J. The Added Value of Small-Molecule Chirality in Technological Applications. *Nat. Rev. Chem.* **2017**, *1* (6), 0045.
(5) Bringmann, G.; Price Mortimer, A. J.; Keller, P. A.; Gresser, M. J.; Garner, J.; Breuning, M. Atroposelective Synthesis of Axially Chiral Biaryl Compounds. *Angew. Chem., Int. Ed.* **2005**, *44* (34), 5384−5427.
(6) Joyce, G. F.; Visser, G. M.; van Boeckel, C. A. A.; van Boom, J. H.; Orgel, L. E.; van Westrenen, J. Chiral Selection in Poly(C)-Directed Synthesis of Oligo(G). *Nature* **1984**, *310* (5978), 602−604.
(7) Honglawan, A.; Beller, D. A.; Cavallaro, M.; Kamien, R. D.; Stebe, K. J.; Yang, S. Topographically Induced Hierarchical Assembly and Geometrical Transformation of Focal Conic Domain Arrays in Smectic Liquid Crystals. *Proc. Natl. Acad. Sci. U. S. A.* **2013**, *110* (1), 34−39.
(8) Araki, T.; Serra, F.; Tanaka, H. Defect Science and Engineering of Liquid Crystals under Geometrical Frustration. *Soft Matter* **2013**, *9* (34), 8107−8120.
(9) Bukusoglu, E.; Bedolla Pantoja, M.; Mushenheim, P. C.; Wang, X.; Abbott, N. L. Design of Responsive and Active (Soft) Materials Using Liquid Crystals. *Annu. Rev. Chem. Biomol. Eng.* **2016**, *7* (1), 163−196.
(10) Xia, Y.; DeBenedictis, A. A.; Kim, D. S.; Chen, S.; Kim, S.-U.; Cleaver, D. J.; Atherton, T. J.; Yang, S. Programming Emergent Symmetries with Saddle-Splay Elasticity. *Nat. Commun.* **2019**, *10* (1), 5104.
(11) Hough, L. E.; Jung, H. T.; Krüerke, D.; Heberling, M. S.; Nakata, M.; Jones, C. D.; Chen, D.; Link, D. R.; Zasadzinski, J.; Heppke, G.; Rabe, J. P.; Stocker, W.; Körblova, E.; Walba, D. M.; Glaser, M. A.; Clark, N. A. Helical Nanofilament Phases. *Science* **2009**, *325* (5939), 456−460.
(12) Salamończyk, M.; Vaupotič, N.; Pociecha, D.; Walker, R.; Storey, J. M. D.; Imrie, C. T.; Wang, C.; Zhu, C.; Gorecka, E. Multi-Level Chirality in Liquid Crystals Formed by Achiral Molecules. *Nat. Commun.* **2019**, *10* (1), 1922.
(13) Dozov, I. On the Spontaneous Symmetry Breaking in the Mesophases of Achiral Banana-Shaped Molecules. *Europhys. Lett.* **2001**, *56* (2), 247−253.
(14) Tkalec, U.; Ravnik, M.; Čopar, S.; Žumer, S.; Muševič, I. Reconfigurable Knots and Links in Chiral Nematic Colloids. *Science* **2011**, *333* (6038), 62−65.
(15) Posnjak, G.; Čopar, S.; Muševič, I. Hidden Topological Constellations and Polyvalent Charges in Chiral Nematic Droplets. *Nat. Commun.* **2017**, *8* (1), 14594.
(16) Nych, A.; Fukuda, J.; Ognysta, U.; Žumer, S.; Muševič, I. Spontaneous Formation and Dynamics of Half-Skyrmions in a Chiral Liquid-Crystal Film. *Nat. Phys.* **2017**, *13* (12), 1215−1220.
(17) Čopar, S.; Kos, Ž.; Emeršič, T.; Tkalec, U. Microfluidic Control over Topological States in Channel-Confined Nematic Flows. *Nat. Commun.* **2020**, *11* (1), 59.
(18) Tortora, L.; Lavrentovich, O. D. Chiral Symmetry Breaking by Spatial Confinement in Tactoidal Droplets of Lyotropic Chromonic Liquid Crystals. *Proc. Natl. Acad. Sci. U. S. A.* **2011**, *108* (13), 5163−5168.
(19) Nych, A.; Ognysta, U.; Muševič, I.; Seč, D.; Ravnik, M.; Žumer, S. Chiral Bipolar Colloids from Nonchiral Chromonic Liquid Crystals. *Phys. Rev. E* **2014**, *89* (6), 062502.
(20) Jeong, J.; Davidson, Z. S.; Collings, P. J.; Lubensky, T. C.; Yodh, A. G. Chiral Symmetry Breaking and Surface Faceting in Chromonic Liquid Crystal Droplets with Giant Elastic Anisotropy. *Proc. Natl. Acad. Sci. U. S. A.* **2014**, *111* (5), 1742−1747.
(21) Jeong, J.; Kang, L.; Davidson, Z. S.; Collings, P. J.; Lubensky, T. C.; Yodh, A. G. Chiral Structures from Achiral Liquid Crystals in Cylindrical Capillaries. *Proc. Natl. Acad. Sci. U. S. A.* **2015**, *112* (15), E1837−E1844.
(22) Nayani, K.; Chang, R.; Fu, J.; Ellis, P. W.; Fernandez-Nieves, A.; Park, J. O.; Srinivasarao, M. Spontaneous Emergence of Chirality in Achiral Lyotropic Chromonic Liquid Crystals Confined to Cylinders. *Nat. Commun.* **2015**, *6* (1), 8067.
(23) Dietrich, C. F.; Rudquist, P.; Lorenz, K.; Giesselmann, F. Chiral Structures from Achiral Micellar Lyotropic Liquid Crystals under Capillary Confinement. *Langmuir* **2017**, *33* (23), 5852−5862.
(24) Lydon, J. Chromonic Review. *J. Mater. Chem.* **2010**, *20* (45), 10071−10099.
(25) Zhou, S.; Nastishin, Yu. A.; Omelchenko, M. M.; Tortora, L.; Nazarenko, V. G.; Boiko, O. P.; Ostapenko, T.; Hu, T.; Almasan, C. C.; Sprunt, S. N.; Gleeson, J. T.; Lavrentovich, O. D. Elasticity of Lyotropic Chromonic Liquid Crystals Probed by Director Reorientation in a Magnetic Field. *Phys. Rev. Lett.* **2012**, *109* (3), 037801.
(26) Zhou, S.; Neupane, K.; Nastishin, Y. A.; Baldwin, A. R.; Shiyanovskii, S. V.; Lavrentovich, O. D.; Sprunt, S. Elasticity, Viscosity, and Orientational Fluctuations of a Lyotropic Chromonic Nematic Liquid Crystal Disodium Cromoglycate. *Soft Matter* **2014**, *10* (34), 6571−6581.
(27) Lohr, M. A.; Cavallaro, M.; Beller, D. A.; Stebe, K. J.; Kamien, R. D.; Collings, P. J.; Yodh, A. G. Elasticity-Dependent Self-Assembly of Micro-Templated Chromonic Liquid Crystal Films. *Soft Matter* **2014**, *10* (19), 3477−3484.
(28) Kim, J. Y.; Nayani, K.; Jeong, H. S.; Jeon, H.-J.; Yoo, H.-W.; Lee, E. H.; Park, J. O.; Srinivasarao, M.; Jung, H.-T. Macroscopic Alignment of Chromonic Liquid Crystals Using Patterned Substrates. *Phys. Chem. Chem. Phys.* **2016**, *18* (15), 10362−10366.
(29) Peng, C.; Guo, Y.; Turiv, T.; Jiang, M.; Wei, Q.-H.; Lavrentovich, O. D. Patterning of Lyotropic Chromonic Liquid Crystals by Photoalignment with Photonic Metamasks. *Adv. Mater.* **2017**, *29* (21), 1606112.
(30) Guo, Y.; Shahsavan, H.; Davidson, Z. S.; Sitti, M. Precise Control of Lyotropic Chromonic Liquid Crystal Alignment through Surface Topography. *ACS Appl. Mater. Interfaces* **2019**, *11* (39), 36110−36117.
(31) Popov, P.; Mann, E. K.; Jákli, A. Thermotropic Liquid Crystal Films for Biosensors and Beyond. *J. Mater. Chem. B* **2017**, *5* (26), 5061−5078.
(32) Park, W.; Wolska, J. M.; Pociecha, D.; Gorecka, E.; Yoon, D. K. Direct Visualization of Optical Activity in Chiral Substances Using a Helical Nanofilament (B4) Liquid Crystal Phase. *Adv. Opt. Mater.* **2019**, *7* (23), 1901399.
(33) Varanytsia, A.; Chien, L.-C. Photoswitchable and Dye-Doped Bubble Domain Texture of Cholesteric Liquid Crystals. *Opt. Lett.* **2015**, *40* (19), 4392−4395.
(34) Ackerman, P. J.; Qi, Z.; Smalyukh, I. I. Optical Generation of Crystalline, Quasicrystalline, and Arbitrary Arrays of Torons in

https://dx.doi.org/10.1021/acscentsci.0c00995
ACS Cent. Sci. XXXX, XXX, XXX−XXX

Confined Cholesteric Liquid Crystals for Patterning of Optical Vortices in Laser Beams. *Phys. Rev. E* **2012**, *86* (2), 021703.
(35) Ackerman, P. J.; Qi, Z.; Lin, Y.; Twombly, C. W.; Laviada, M. J.; Lansac, Y.; Smalyukh, I. I. Laser-Directed Hierarchical Assembly of Liquid Crystal Defects and Control of Optical Phase Singularities. *Sci. Rep.* **2012**, *2* (1), 414.
(36) Kim, D. S.; Čopar, S.; Tkalec, U.; Yoon, D. K. Mosaics of Topological Defects in Micropatterned Liquid Crystal Textures. *Sci. Adv.* **2018**, *4* (11), eaau8064.
(37) Suh, A.; Yoon, D. K. Nanoscratching Technique for Highly Oriented Liquid Crystal Materials. *Sci. Rep.* **2018**, *8* (1), 9460.
(38) Cha, Y. J.; Park, S. M.; You, R.; Kim, H.; Yoon, D. K. Microstructure Arrays of DNA Using Topographic Control. *Nat. Commun.* **2019**, *10* (1), 2512.
(39) McGinn, C. K.; Laderman, L. I.; Zimmermann, N.; Kitzerow, H.-S.; Collings, P. J. Planar Anchoring Strength and Pitch Measurements in Achiral and Chiral Chromonic Liquid Crystals Using 90-Degree Twist Cells. *Phys. Rev. E* **2013**, *88* (6), 062513.
(40) Martinez, A.; Collings, P. J.; Yodh, A. G. Brownian Dynamics of Particles "Dressed" by Chiral Director Configurations in Lyotropic Chromonic Liquid Crystals. *Phys. Rev. Lett.* **2018**, *121* (17), 177801.
(41) Ravnik, M.; Žumer, S. Landau−de Gennes Modelling of Nematic Liquid Crystal Colloids. *Liq. Cryst.* **2009**, *36* (10−11), 1201−1214.
(42) Yi, Y.; Clark, N. A. Orientation of Chromonic Liquid Crystals by Topographic Linear Channels: Multi-Stable Alignment and Tactoid Structure. *Liq. Cryst.* **2013**, *40* (12), 1736−1747.
(43) Smalyukh, I. I.; Lavrentovich, O. D.; Kuzmin, A. N.; Kachynski, A. V.; Prasad, P. N. Elasticity-Mediated Self-Organization and Colloidal Interactions of Solid Spheres with Tangential Anchoring in a Nematic Liquid Crystal. *Phys. Rev. Lett.* **2005**, *95* (15), 157801.
(44) Ogolla, T.; Nashed, S. B.; Collings, P. J. Pitch Measurements in Chiral Lyotropic Chromonic Liquid Crystals. *Liq. Cryst.* **2017**, *44* (12−13), 1968−1978.
(45) Turiv, T.; Koizumi, R.; Thijssen, K.; Genkin, M. M.; Yu, H.; Peng, C.; Wei, Q.-H.; Yeomans, J. M.; Aranson, I. S.; Doostmohammadi, A.; Lavrentovich, O. D. Polar Jets of Swimming Bacteria Condensed by a Patterned Liquid Crystal. *Nat. Phys.* **2020**, *16* (4), 481−487.
(46) Hentschel, M.; Schäferling, M.; Duan, X.; Giessen, H.; Liu, N. Chiral Plasmonics. *Sci. Adv.* **2017**, *3* (5), e1602735.
(47) Soni, V.; Bililign, E. S.; Magkiriadou, S.; Sacanna, S.; Bartolo, D.; Shelley, M. J.; Irvine, W. T. M. The Odd Free Surface Flows of a Colloidal Chiral Fluid. *Nat. Phys.* **2019**, *15* (11), 1188−1194.

https://dx.doi.org/10.1021/acscentsci.0c00995
ACS Cent. Sci. XXXX, XXX, XXX−XXX